quantum beam science

MDPI

Supplementary Information

Laser Peening Analysis of Aluminum 5083: A Finite Element Study

Ali Tajyar [1], Noah Holtham [1], Nicholas Brooks [1], Lloyd Hackel [2], Vincent Sherman [2], Ali Beheshti [3] and Keivan Davami [1,*]

[1] Department of Mechanical Engineering, The University of Alabama, Tuscaloosa, AL 35487, USA; atajyar@ua.edu (A.T.); nholtham@crimson.ua.edu (N.H.); nabrooks1@crimson.ua.edu (N.B.)

[2] Curtiss Wright Surface Technologies, Metal Improvement Company, Livermore, CA 94551, USA; Lloyd.Hackel@cwst.com (L.H.); Vincent.Sherman@cwst.com (V.S.)

[3] Department of Mechanical Engineering, George Mason University, Fairfield, VA 22030, USA; abehesh@gmu.edu

* Correspondence: kdavami@eng.ua.edu

S1. Simulation of the laser peening process

S1.1. Pressure loading condition

In current simulation model, similar to most of the literature studies [1–3], the pressure load induced by LP was defined as a function of elapsed time. As can be seen in Figure S1, slightly after the LP process starts, the pressure rises to a maximum pressure during the laser pulse. Once the maximum pressure is achieved, the pressure rapidly goes back down. Two main components of temporal pressure function, *P(t)*, are (1) the pulse time and (2) the peak pressure. It has been shown that one can approximate the *P(t)* with a 6th order polynomial function [4,5]. Thanks to presence of the dielectric transparent material, the pressure pulse time in the confined ablation mode, typically last two to three times longer than the length of laser pulse [6,7]. In this report, a pressure pulse three times longer than the 18 ns laser pulse duration was considered. Since it is very challenging to evaluate the spatial distribution of the pressure pulse experimentally, commonly, particularly for a pulse with a square geometry, a uniform distribution at the laser impact region is considered [8–11]. This approach was also implemented here where the loaded pressures were applied uniformly at the entire peened area.

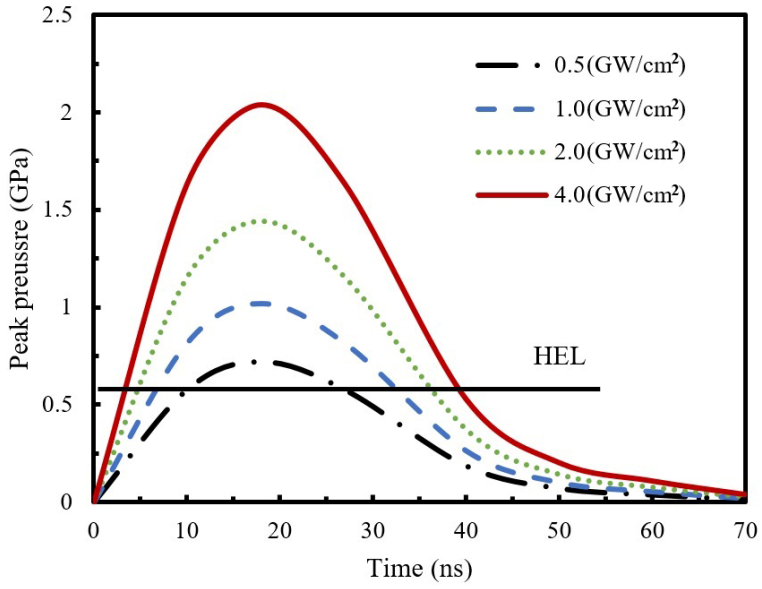

Figure S1. Temporal pressure profile.

The peak pressure can be calculated via Equation (1) [12–14]:

$$P\ (\mathrm{GPa}) = 0.01\sqrt{\frac{\alpha}{2\alpha+3}}\sqrt{Z\ (\mathrm{g/cm^2 s})}\sqrt{I_0\ (\mathrm{GW/cm^2})} \quad (1)$$

where P is the peak pressure, I_0 is the laser power density and α is the efficiency of the interaction in the range of 0.2 to 0.5, typically. Z denotes the combined shock impedance defined by:

$$\frac{2}{Z} = \frac{1}{Z_1} + \frac{1}{Z_2} \quad (2)$$

where Z_1 and Z_2 are the shock impedance of the target material and the confining overlay, respectively.

With the propagation of the pressure wave into the specimen, the material becomes plastically deformed up to a depth at which the peak pressure of the wave becomes smaller than the metal's HEL [15–17]. At HEL, the transitions from a purely elastic state to an elastic-plastic state happens in a solid due to a strong pressure wave. The HEL is related to dynamic yield strength, σ_y, and Poisson's ratio, ν, of the material through $HEL = \frac{1-\nu}{1-2\nu}\sigma_y$. According to the Poisson's effect, where material tends to expand in directions perpendicular to the direction of compression, when the pressure wave deforms the material surface and subsurface, the metal spreads transversely to conserve volume. The neighboring material resists the expansion, generating a compressive stress at the surface and subsurface regions. In order for the specimen to stay in equilibrium, a tensile field is also induced where its distribution depends on the geometry of specimen. Up to the depth where the pressure wave exceeds the HEL, high strain rate plastic deformation results in the generation of entangled dislocations with a large density. Of course, when the peak pressure of the stress wave is less than the HEL, no plastic strains occur. As shown in Figure S1, all of the selected power densities in this research produce peak pressures (P_{Peak} of 0.72 GPa to 2.44 GPa) which are more than the HEL of Al 5083 (0.57 GPa).

S1.2. Solution time

Two analysis steps with proper solution times were considered to obtain the efficient and accurate results. By considering a solution time much longer than the length of the pressure pulse, enough time is given to the reflection and interaction of the pressure waves that are traveling in the specimen. This of importance since it adds to the accuracy of the resultant dynamic response of the material in the first step [11]. Therefore, it is vital to determine the optimum solution time of the dynamic response that gives enough time to all the plastic deformation to take place. When the wave propagates in the material, a conversion of the internal energy to elastically stored energy, plastically dissipated energy, and artificial strain energy occurs [18]. Figure S2a illustrates the changes in the internal energy in the first step of the simulation during the dynamic response of the material. While the internal energy initially increases, reaches its maximum value, and then slowly decreases and becomes stable after 4500 ns, the plastically dissipated energy increases and reaches a saturation level in less than 500 ns. This indicates that it takes approximately 4500 ns for all the plastic deformation to occur. Therefore, with an addition of 500 ns to increase the reliability margin, a 5000 ns time period was chosen as the solution time for the dynamic analysis [19]. The surface residual stresses obtained in the second step have been shown in Figure S2b for different step times. These stresses were measured along a line from the center to the edge of the laser spot. As seen here, there is no observable changes after 100,000 ns. Therefore, the second step time was considered to be 100,000 ns to obtain an equilibrium of the stresses and an accurate residual stress field [1,8].

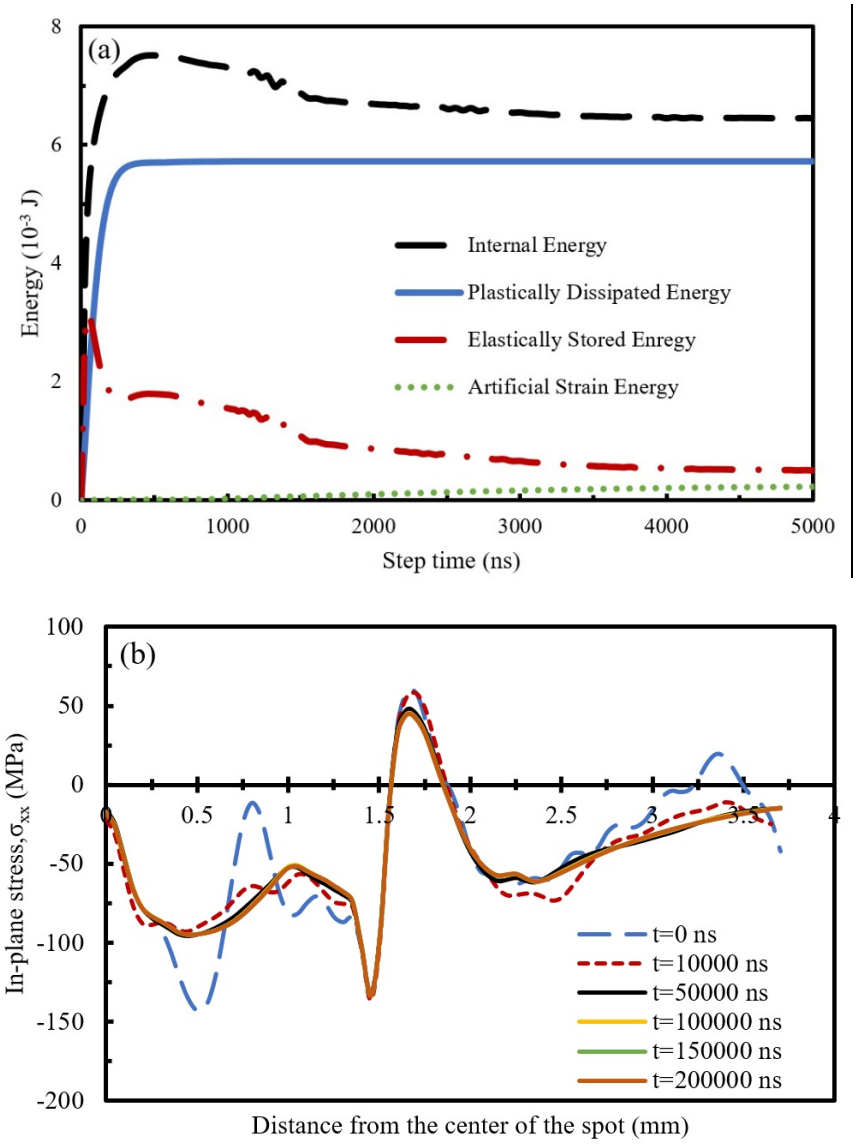

Figure S2. (**a**) History of the internal energy, elastically stored energy, plastically dissipated energy and artificial strain energy during the first step (**b**) In-plane stress profiles (σ_{xx}) versus distance from the center of spot at different calculation times during the second step (A dynamic state towards a residual state). It can be concluded that a quasi-equilibrium state is reached above 100,000 ns.

S2. Residual Stress Measurement

Diffracted X-rays were collected for a given family of planes {*hkl*} and the lattice spacing, $d^{\{hkl\}}$ was determined via Bragg's Law. The strain ($\varepsilon_{\varphi\psi}^{\{hkl\}}$) was then calculated from the change in lattice spacing by Equation (3):

$$\varepsilon_{\varphi\psi}^{\{hkl\}} = \frac{d_{\varphi\psi}^{\{hkl\}} - d_0^{\{hkl\}}}{d_0^{\{hkl\}}} \quad (3)$$

where $d_{\varphi\psi}^{\{hkl\}}$ is the lattice spacing measured at a sample orientation denoted by φ and Ψ angels, and $d_0^{\{hkl\}}$ is the lattice spacing of the unstrained sample. For the cosα method, strains are measured by comparing the distorted Debye ring of the stressed sample with the perfectly circular ring from a stress-free sample (Figure S3) [20]. Equation (4) shows how strain ($\bar{\varepsilon}_{\alpha}^{\{hkl\}}$) is calculated from four points located at 90° on the Debye ring ($\varepsilon_{\alpha}^{\{hkl\}}$, $\varepsilon_{\pi+\alpha}^{\{hkl\}}$, $\varepsilon_{-\alpha}^{\{hkl\}}$, $\varepsilon_{\pi-\alpha}^{\{hkl\}}$):

$$\bar{\varepsilon}_{\alpha}^{\{hkl\}} = \frac{1}{2}\left[\left(\varepsilon_{\alpha}^{\{hkl\}} - \varepsilon_{\pi+\alpha}^{\{hkl\}}\right) + \left(\varepsilon_{-\alpha}^{\{hkl\}} - \varepsilon_{\pi-\alpha}^{\{hkl\}}\right)\right] \quad (4)$$

By varying α from 0° to 90°, stress can then be calculated as a linear function of regression between $\bar{\varepsilon}_{\alpha}^{\{hkl\}}$ and cosα by Equation (5),

$$\sigma_{\varphi} = \frac{E}{1+\nu} \frac{1}{\sin 2\eta \cdot \sin 2\Psi_0} \frac{\partial \bar{\varepsilon}_{\alpha}^{\{hkl\}}}{\partial \cos\alpha} \quad (5)$$

where E, υ and 2η are the Young's modulus, the Poisson's ratio of the material and the semi-angle of the Debye ring, respectively [21]. The angles of φ, η, Ψ and α are shown in Figure S3.

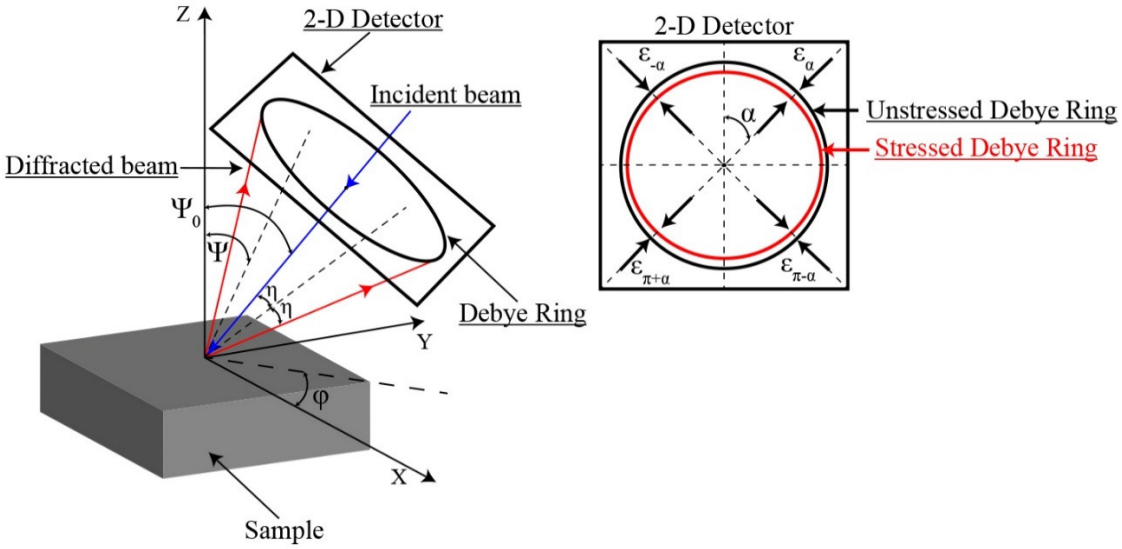

Figure S3. Debye ring measurement schematic.

References:

[1] P. Peyre, I. Chaieb, and C. Braham, "FEM calculation of residual stresses induced by laser shock processing in stainless steels," *Model. Simul. Mater. Sci. Eng.*, vol. 15, no. 3, pp. 205–221, Apr. 2007, doi: 10.1088/0965-0393/15/3/002.

[2] M. Achintha and D. Nowell, "Eigenstrain modelling of residual stresses generated by laser shock peening," *J. Mater. Process. Technol.*, vol. 211, no. 6, pp. 1091–1101, Jun. 2011, doi: 10.1016/j.jmatprotec.2011.01.011.

[3] X. Zhang *et al.*, "Modeling of residual stress field induced in Ti-6Al-4V alloy plate by two sided laser shock processing," *Surf. Coatings Technol.*, vol. 280, pp. 163–173, Oct. 2015, doi: 10.1016/j.surfcoat.2015.09.004.

[4] M. P. Sealy and Y. B. Guo, "Surface integrity and process mechanics of laser shock peening of novel biodegradable magnesium-calcium (Mg-Ca) alloy," *J. Mech. Behav. Biomed. Mater.*, vol. 3, no. 7, pp. 488–496, Oct. 2010, doi: 10.1016/j.jmbbm.2010.05.003.

[5] L. Berthe, R. Fabbro, P. Peyre, L. Tollier, and E. Bartnicki, "Shock waves from a water-confined laser-generated plasma," *J. Appl. Phys.*, vol. 82, no. 6, pp. 2826–2832, Sep. 1997, doi: 10.1063/1.366113.

[6] D. Devaux, R. Fabbro, L. Tollier, and E. Bartnicki, "Generation of shock waves by laser-induced plasma in confined geometry," *J. Appl. Phys.*, vol. 74, no. 4, pp. 2268–2273, Aug. 1993, doi: 10.1063/1.354710.

[7] L. Berthe, R. Fabbro, P. Peyre, and E. Bartnicki, "Wavelength dependent of laser shock-wave generation in the water-confinement regime," *J. Appl. Phys.*, vol. 85, no. 11, pp. 7552–7555, Jun. 1999, doi: 10.1063/1.370553.

[8] R. Bikdeloo, G. H. Farrahi, A. Mehmanparast, and S. M. Mahdavi, "Multiple laser shock peening effects on residual stress distribution and fatigue crack growth behaviour of 316L stainless steel," *Theor. Appl. Fract. Mech.*, vol. 105, p. 102429, Feb. 2020, doi: 10.1016/j.tafmec.2019.102429.

[9] K. Ding and L. Ye, "Simulation of multiple laser shock peening of a 35CD4 steel alloy," *J. Mater. Process. Technol.*, vol. 178, no. 1–3, pp. 162–169, Sep. 2006, doi: 10.1016/j.jmatprotec.2006.03.170.

[10] H. Chen, A. Feng, J. Li, T. Jia, and Y. Liu, "Effects of Multiple Laser Peening impacts on Mechanical Properties and Microstructure Evolution of 40CrNiMo Steel," *Journal of Materials Engineering and Performance*, vol. 28, no. 5. Springer New York

LLC, pp. 2522–2529, May-2019, doi: 10.1007/s11665-019-04034-x.

[11] Y. Hu, Z. Yao, and J. Hu, "3-D FEM simulation of laser shock processing," *Surf. Coatings Technol.*, vol. 201, no. 3–4, pp. 1426–1435, Oct. 2006, doi: 10.1016/j.surfcoat.2006.02.018.

[12] P. BALLARD, J. FOURNIER, R. FABBRO, and J. FRELAT, "Residual Stresses Induced By Laser-Shocks," *Le J. Phys. IV*, vol. 01, no. C3, pp. C3-487-C3-494, Oct. 1991, doi: 10.1051/jp4:1991369.

[13] R. Fabbro, J. Fournier, P. Ballard, D. Devaux, and J. Virmont, "Physical study of laser-produced plasma in confined geometry," *J. Appl. Phys.*, vol. 68, no. 2, pp. 775–784, 1990, doi: 10.1063/1.346783.

[14] P. Peyre and R. Fabbro, "Laser shock processing: a review of the physics and applications," *Opt. Quantum Electron.*, vol. 27, no. 12, pp. 1213–1229, Dec. 1995, doi: 10.1007/BF00326477.

[15] Y. Wei *et al.*, "Anomalous shear band characteristics and extra-deep shock-affected zone in Zr-based bulk metallic glass treated with nanosecond laser peening," *Sci. Rep.*, vol. 7, no. 1, pp. 1–7, Mar. 2017, doi: 10.1038/srep43948.

[16] Y. Wei *et al.*, "Anomalous shear band characteristics and extra-deep shock-affected zone in Zr-based bulk metallic glass treated with nanosecond laser peening," *Sci. Rep.*, vol. 7, Mar. 2017, doi: 10.1038/srep43948.

[17] A. H. Clauer and D. F. Lahrman, "Laser shock processing as a surface enhancement process," *Key Eng. Mater.*, vol. 197, pp. 121–142, 2001, doi: 10.4028/www.scientific.net/kem.197.121.

[18] *ABAQUS user's manual (2020)*. 2020.

[19] X. L. Wei and X. Ling, "Numerical modeling of residual stress induced by laser shock processing," in *Applied Surface Science*, 2014, vol. 301, pp. 557–563, doi: 10.1016/j.apsusc.2014.02.128.

[20] T. Sasaki and Y. Hirose, "INFLUENCE OF IMAGE PROCESSING CONDITIONS OF DEBYE SCHERRER RING IMAGES IN X-RAY STRESS MEASUREMENT USING AN IMAGING PLATE."

[21] D. Delbergue, D. Texier, M. Levesque, P. Bocher, D. Texier, and M. Lévesque, "Comparison of Two X-Ray Residual Stress Measurement Methods: Sin2 ψ and Cos α, Through the Determination of a Martensitic Steel X-Ray Elastic Constant," in *Residual Stresses 2016*, 2017, vol. 2, pp. 55–60, doi: 10.21741/9781945291173-10.